Elastomer-Alginate Interface for High-Power and High-Energy Zn Metal Anodes

*Qun Liu, Yu Wang, Xiaodan Hong, Rui Zhou, Zhen Hou, Biao Zhang**

Qun Liu, Rui Zhou, Zhen Hou, Biao Zhang

Department of Applied Physics, The Hong Kong Polytechnic University, Hung Hom, Hong Kong 999077, China. E-mail: biao.ap.zhang@polyu.edu.hk

Yu Wang

Department of Electronic and Information Engineering, The Hong Kong Polytechnic University, Hung Hom, Hong Kong 999077, China.

Xiaodan Hong

Department of Applied Physics, School of Science, Aalto University, Espoo, Helsinki 02150, Finland.

Keywords: Elastomer, Zn-alginate, corrosion, dendrites, zinc-metal battery

Abstract: Spontaneous corrosion and uncontrolled dendrites accumulation of Zn would rapidly degrade zinc-metal battery performance. Artificial interfaces have been widely fabricated on Zn metal anodes, yet most interfaces are detrimental to ion transfer and hardly adapt to spatial changes during Zn plating/stripping. Herein, a hybrid interface, consisting of thermoplastic polyurethane (TPU) fiber matrix and Zn-alginate (ZA) filler, is designed, which serves as a physical barrier between anode and electrolyte to inhibit the side reactions. Encouragingly, ZA regulates Zn^{2+} transport and endows uniform Zn deposition by inducing the plating/stripping underneath the hybrid interface. At the same time, the TPU frame acts as a super-elastic constraint to further suppress rampant dendrite evolution and accommodate a large amount of deposited Zn. Consequently, the interface-protected Zn anode delivers high cycling stability (1200 h at 5 mA cm^{-2}/5 mAh cm^{-2}; 500 h at 10 mA cm^{-2}/10 mAh cm^{-2}), realizing an exceptional cumulative capacity of over 6000 mAh cm^{-2}. This enhancement is well maintained in the full

cell when coupled with a vanadium-based cathode. The unique matrix-filler architecture and mechanistic insights unraveled in this study would provide a general principle in designing functional interfaces for metal anodes.

1. Introduction

Li-ion batteries with high energy density currently occupy most of the portable electronic battery market. Several key factors, such as shortage of lithium resources, high production costs, and flammable organic electrolytes, restrict their application in specific scenarios like stationary energy storage.[1] To this end, vigorous research attempts are ongoing to develop aqueous rechargeable Zn-ion batteries (ZIBs) owing to the impressive features of Zn metal, including low redox potential (-0.76 V versus the standard hydrogen electrode), high theoretical capacity (820 mAh g^{-1}), natural abundance, and environmental compatibility.[2] However, Zn anode is poised to undergo severe corrosion, hydrogen evolution, and uncontrollable dendrite growth in the aqueous electrolyte, all of which resonate with each other leading to inevitable short circuit and unsatisfactory battery life.[3]

Considerable efforts have been devoted to the host structure design and electrolyte optimization for circumventing Zn anode stability issues, which significantly improve the lifespan.[4] Alternatively, surface coating, which acts as an artificial interface, is a direct approach to separate the anode from the electrolyte. It is not restricted by the availability of electrolytes and does not entail complex electrode modification. In this respect, coating layers based on ZnSe,[5] ZnO,[6] ZnF_2,[7] TiO_2,[8] $CaCO_3$,[9] $BaTiO_3$,[10] Tin[11], Indium[12] and $ZnMoO_4$[13] have been adopted to stabilize Zn anode by preventing the corrosion of Zn metal from producing byproducts. Nevertheless, the stability of such coatings at high current rates and large cycling capacities remains a grand challenge. According to Sand's model,[14] a high current density would provoke the dendrite formation. Meanwhile, the larger area capacity

accelerates the volume change and dendrite growth of Zn anodes. The above inorganic rigid interfaces could hardly accommodate the deformation and are vulnerable to rupture and failure. Therefore, elastic polymers including PAN,[15] PDMS,[16] and PVDF[17] have been applied to circumvent the challenges, which provide excellent mechanical support and significantly boost the Zn anode stability. In particular, elastomers with stable chemical properties and adaptability to various deformations are handy candidates. They are easily electrospun into a porous film which exhibits superior elasticity up to 500%.[18] Despite the apparent advantages of the elastomer films in mechanical stability, they have never been employed to fabricate functional interfaces on Zn metal anodes. The reason may lie in their hydrophobicity nature and poor ionic conductivity.[19]

Herein, a hybrid interface is developed by infiltrating Zn-alginate (ZA) into porous thermoplastic polyurethane (TPU) networks for realizing concurrently high-current-rate and large-capacity Zn metal anodes. The TPU elastomer provides mechanical support allowing a large amount of Zn deposition. The ZA is prepared using commercial-available sodium alginate as the precursor through a facile ion exchange between Zn and Na ions. The resulting ZA facilitates the ion transfer, thus effectively protecting the Zn metal from corrosion without sacrificing the kinetics. However, the neat ZA hydrogel electrolyte cannot sustain the large-capacity cycling due to the poor mechanical stability (**Figure S1**). Combining the benefits of TPU and ZA, the modified Zn anode (denoted as Zn@TPZA) demonstrates an enhanced battery lifespan at high current densities (up to 1200 h at 5 mA cm^{-2}/5 mAh cm^{-2}), achieving one of the highest cumulative cycling capacities so far among all the interface-modified Zn metal anodes.

2. Results and Discussions

2.1. Synthesis and Characterization of Zn@TPZA Anode.

Figure 1a schematically illustrates the synthetic procedure for the hybrid layer on Zn foil. Firstly, the intertwined TPU fibers with a diameter range between 1-3 μm are produced by electrospinning directly on a cleaned Zn foil (**Figure 1b**). The microfibers exhibit smooth surfaces and merged junctions, which are conducive to their mechanical properties.[23] As depicted in **Figure 1c**, the TPU matrix demonstrates superior flexibility, which can be bent, twisted, folded, curled, etc. In particular, it displays an excellent tensile strain of over 400% and recovers rapidly once the stress is unloaded (**Figure 1d**). To examine the compatibility with the electrolyte, the TPU film is immersed in 2M $ZnSO_4$ electrolyte for 30 days. It is a delight to find the TPU film maintains its original morphology (**Figure S2a**) and elasticity. None of the impure phases is detected in the X-ray diffraction (XRD) pattern (**Figure S2b**), suggesting the negligible side reactions and the stability of TPU in an acidic electrolyte. This is also confirmed by the nearly unchanged bonds vibration and elements status of the TPU before and after soaking in the electrolyte (**Figure S2c-f**). Considering the inhomogeneous Zn deposition and subsequent preferential growth would result in the stress concentration on the interface,[20] we investigate the integrity of the TPU film under increased local force. As shown in **Figure 1e**, despite dramatic deformation, TPU film cannot be pierced subject to the indentation of a sharp tip and fully returns to the initial state after releasing the force.

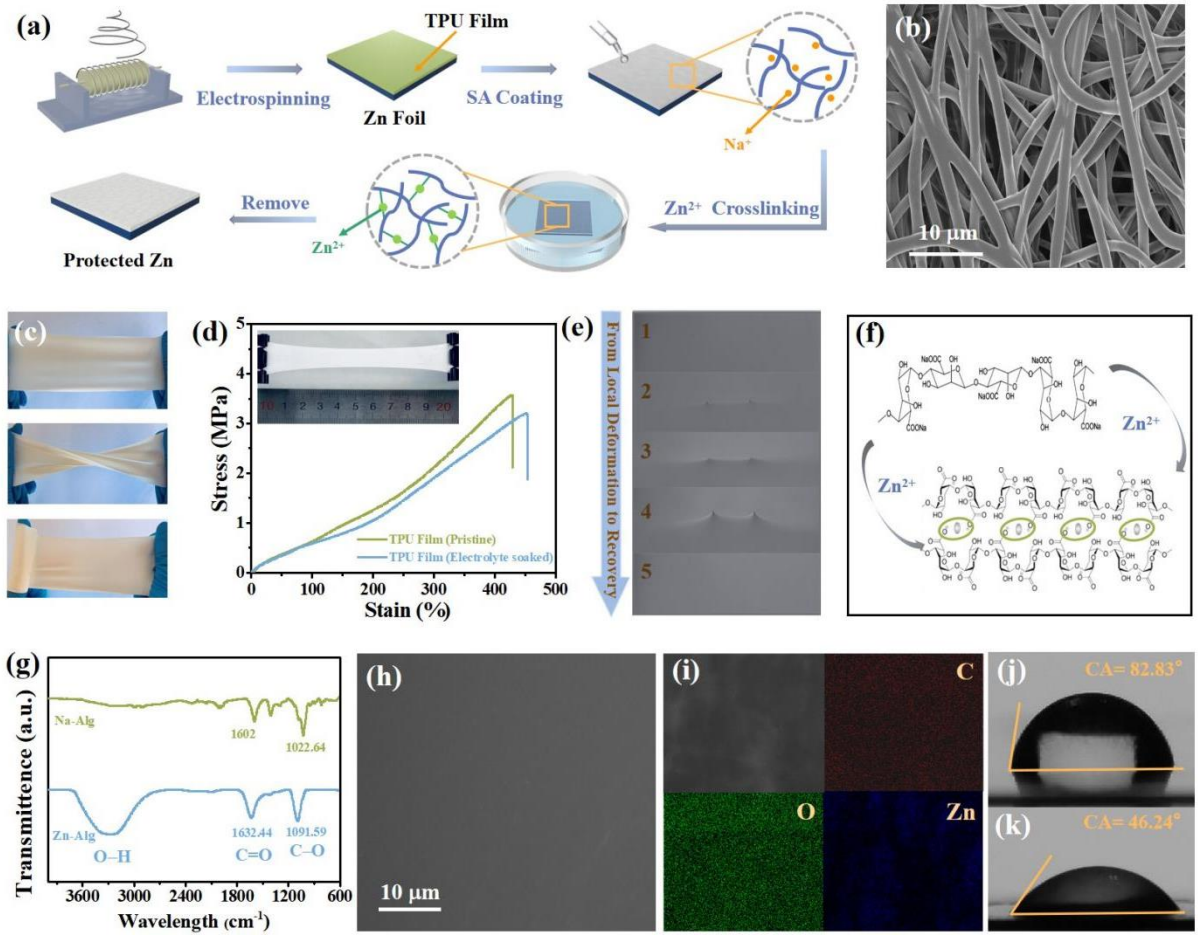

Figure 1. Synthesis and characterization of Zn@TPZA. (a) Illustration of the procedure to fabricate hybrid interface; (b) Scanning electron microscopy (SEM) image of TPU nanofibers; (c) Flexibility demonstration of TPU film; (d) The stress-strain curve of TPU film (inset shows the optical image under stretched status); (e) Local deformation test of TPU film; (f) Crosslinking mechanism of Zn-Alg formation; (g) FT-IR spectrum of Na-Alg and Zn-Alg; (h) SEM image and (i) elemental mapping of the Zn@TPZA; Digital images of the contact angle tests of 2 M $ZnSO_4$ on (j) bare Zn and (k) Zn@TPZA.

An ideal interface should possess not only excellent mechanical stability but also outstanding ionic conductivity for fast charge transfer. To boost the ionic conductivity of Zn ions, the TPU film deposited on Zn foil is infiltrated by 2 wt% sodium alginate (Na-Alg) precursor and subsequently immersed into 2 M $ZnSO_4$ electrolyte to crosslink for 12 h. The mechanism is shown in **Figure 1f**. Na-Alg is a copolymer consisting of D-mannuronic acid (M)

and L-guluronic acid (G) as structural units.[21] Zn^{2+} ions replace Na^{+} in the G unit by ion exchange and are sandwiched between alginate molecules to form an egg-shell structure. As the reaction proceeds, G units continue to accumulate and end up forming the Zn-Alg network. The successful crosslinking is verified by Fourier transform infrared spectroscopy (FT-IR, **Figure 1g**). After the formation of coordinated bonds between Zn^{2+} and carboxylate groups, the asymmetric C=O stretching vibration peak located at 1602 cm^{-1} of the Na-Alg chains shifts to 1632.44 cm^{-1} due to the change of cation radius and charge density.[22] Meanwhile, the peak at 1091.59 cm^{-1} is assigned to C-O stretching vibration while the band in 3309.79 cm^{-1} corresponds to the O-H stretching vibrations of hydrogen bonds.[23]

The Zn@TPZA with different amounts of ZA is examined to reveal the structural evolution. The ZA filler is gradually permeated into the TPU framework to form a compact and smooth layer (**Figure S3**). The as-obtained hybrid interface displays a dense surface without profound protuberances (**Figure 1h,** and **Figure S4**), thanks to the self-adaptation of the interface to the Zn substrate. The elemental mapping of Zn@TPZA suggests the homogeneous distribution of Zn, C, and O, further indicating Na-Alg is uniformly crosslinked by Zn^{2+} (**Figure 1i**). The X-ray photoelectron spectroscopy (XPS) confirms the presence of Zn element in Zn-Alg, which shows the $Zn2p_{3/2}$ at 1022.08 eV (**Figure S5**).[24] The cross-sectional view of Zn@TPZA (**Figure S6**) shows the thickness is around 10 μm. The wettability of the Zn anode surface plays a critical role in the reversible Zn plating/stripping and the interfacial ion transfer.[25] Pristine Zn foil displays the static contact angle of 83° in 2 M $ZnSO_4$ electrolyte (**Figure 1j**). After being coated by hydrophobic TPU, the contact angle increases to 111° (**Figure S7**). In contrast, the contact angle of Zn@TPZA drops sharply to 46° (**Figure 1k**), a reflection of the significantly boosted wettability.

2.2 Surface Protection and Zn Deposition Regulation.

One of the essential roles of the interface is to protect the Zn anode from corrosion. We probe the Zn surface functionality with/without protective interface during the static rest and cycling process, as shown in **Figure 2a**. The Zn electrodes are immersed into a 2 M $ZnSO_4$ electrolyte. After being soaked for 30 days, randomly oriented hexagonal micro-sheets in various sizes can be found on the bare Zn surface due to the inherent chemical instability from the thermodynamic point of view (**Figure 2b**). By contrast, the surface of Zn@TPZA maintains its pristine morphology without detecting byproducts (**Figure 2c**). The flaky byproducts observed on the bare Zn surface are identified as zinc hydroxide sulphate hydrate ($Zn_4SO_4(OH)_6 \cdot 3H_2O$) (**Figure 2d**). In detail, the hydrogen is evolved because of the reduction of H_2O by Zn metal, which consumes the H^+ in the initial acidic electrolyte and increases the pH value. The inert $Zn_4SO_4(OH)_6 \cdot 3H_2O$ generates afterward and covers the surface. Noted that such a reaction could hardly be self-terminate as the byproducts are not compact to separate the Zn metal and the electrolyte. Thus, the Zn metal would be gradually depleted, accompanied by the accumulation of the byproducts. Consequently, the intensity of characteristic diffraction peaks of $Zn_4SO_4(OH)_6 \cdot 3H_2O$ is much stronger than those of pristine Zn after 30 days. In contrast, only a tiny peak of the byproduct is observed in the XRD pattern of Zn@TPZA after immersion in the electrolytes for 30 days, suggesting the solid capability of as-fabricated interfaces in inhibiting the side reactions. Furthermore, it can be observed that bare Zn without a protective layer almost fully loses the (002) peak after soaking in the electrolyte for 30 days. The (002) plane is close-packed with the lowest surface energy. It is easy to absorb OH^- when soaked in electrolyte for a long time, and oxygen corrosion reaction occurs more significantly. Thanks to the presence of the TPZA layer, the corrosion is largely inhibited. The electrochemical window is also examined on bare and protected Zn anodes under 2 M $ZnSO_4$ electrolyte (**Figure S8**). It confirms that the protected layer could delay the oxygen evolution and hydrogen evolution reactions to improve cell reliability.

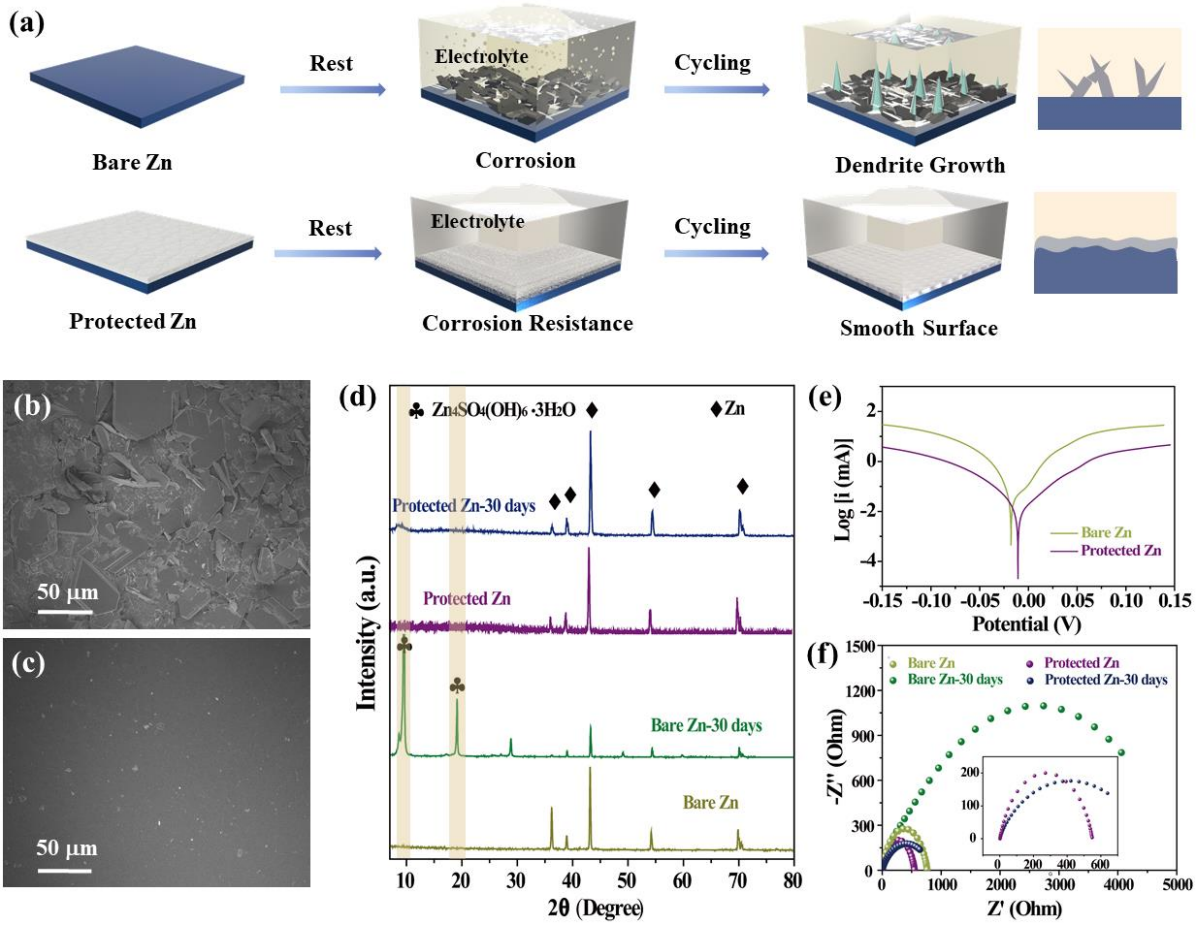

Figure 2. The corrosion characterization of Zn and Zn@TPZA in 2 M $ZnSO_4$ electrolyte. (a) Schematic of static rest and cycling process for Zn and Zn@TPZA anodes; SEM images of (b) bare Zn and (c) Zn@TPZA after immersion in 2 M $ZnSO_4$ electrolyte for 30 days, and (d) the corresponding XRD patterns; (e) Linear polarization curves of bare Zn and Zn@TPZA anodes; (f) EIS of bare Zn and Zn@TPZA before and after immersion in 2 M $ZnSO_4$ electrolyte.

The linear polarization tests (**Figure 2e**) are further conducted to elucidate the corrosion behavior. The protected Zn displays a lower corrosion current and an increased corrosion potential than the bare Zn anode, yielding a reduced corrosion tendency that explains the restrained parasite reactions observed before. The accumulated byproducts on the surface of the anode also hinder Zn ion transfer. As disclosed in the Nyquist plots in **Figure 2f**, the impedance of the bare Zn cell manifests a remarkable increase after being soaked in the electrolyte. In contrast, the impedance of the protected Zn cell shows a slight change. It is noteworthy that the

Zn@TPZA has a lower resistance than bare Zn at the initial stage, proving the interface does not harm the ionic conductivity. Instead, it slightly increases the Zn ion transfer kinetics due possibly to the intimate contact between the self-adaptive interface and the Zn substrate.[6]

To further evaluate the suitability of TPZA as an artificial coating, the electronic conductivity and ionic conductivity are examined. The electronic conductivity of TPZA layer is $1.5*10^{-10}$ S cm^{-1} (**Figure S9**), which is comparable to other artificial SEIs, such as Poly-ZnP_2O_6/ZnF_2 ($7.6*10^{-5}$ S cm^{-1})[26] and $Zn_3(PO_4)_2{\cdot}4H_2O$ ($1.1*10^{-8}$ S cm^{-1})[27]. The high electronic resistance of the TPZA layer is critical for establishing the necessary potential gradient across the artificial coating to drive Zn^{2+} diffusion. In addition, the electrolyte-soaked ZA and TPZA feature good ionic conductivity. As shown in **Figure 3a**, it is impressive that the ZA membrane exhibits an excellent ionic conductivity of 19.8 mS cm^{-1}, which is slightly higher than that of the liquid electrolyte (13.4 mS cm^{-1}). The integration of ZA and TPU only slightly decrease the value to 16.4 mS cm^{-1} for the TPZA membrane. The performance is comparable to other reported liquid-soaked polymer electrolytes (**Table S1**).

Symmetric cells with the bare and protected Zn as electrodes are assembled to examine the morphology evolution during the deposition process. An extremely high current density of 10 mA cm^{-2} is adopted, which is required for practical application to achieve high-power ZIBs but remains challenging due to the aggravated dendrite initiation. The morphology of the electrodes is systematically investigated at increased deposition amounts. As shown in **Figure 3b**, large Zn flakes with sharp edges are presented after 60 mins, potentially penetrating the separator and resulting in short-circuit. We speculate the Zn ions would be preferentially deposited on the protrusions of the bare Zn (**Figure S2**) because of the tip-enhanced electric field, which triggers the inhomogeneous Zn growth. We also examine the Zn morphology under the protection of TPZA, which is peeled off peeling off for direct visulization. Although the Zn surface would be partly impaired during the sample preparation, the protected Zn anode still presents a much flat and compact morphology (**Figure 3c**) compared to Zn anode without

TPZA interface. The 3D height images show a much rougher surface of the bare Zn than that of the protected one after 60 mins (10 mAh) Zn deposition (**Figure 3d-e**). The maximum height differences are 7.1 μm and 0.34 μm for the anode without and with the TPZA layer, respectively.

To corroborate the underlying mechanism for the distinct Zn growth behavior, we first use XRD to examine whether side reactions occur. Surprisingly, the $Zn_4SO_4(OH)_6 \cdot 3H_2O$ byproducts are detected on the bare Zn after merely 60 mins deposition (**Figure S10**). As discussed before, such a parasite reaction will erode the Zn surface and increase the surface roughness, promoting inhomogeneous Zn nucleation. In comparison, no apparent corrosion occurs on Zn@TPZA, similar to the long-time rest test results.

Apart from anti-corrosion, the interface also benefits the smooth Zn growth by homogenizing the electric field. Since the Zn^{2+} could transfer along the polymer chains of Zn-Alg, "tip effects" caused by the protrusions on the surface are largely shielded, as verified by the theoretical simulation (**Figure 3f-g**), due to the combined effects of both interface and abundant seeds. We construct a second model to explore the shielding effect of the interface alone by assuming the same number of Zn seeds are produced (**Figure S11**). In this case, we could still find the more homogeneous electric field with the TPZA, compared to the heavily centralized electric field surrounding the deposited Zn tips in the absence of the TPZA. Chronoamperometry test in symmetric cells is taken to certify the theoretical results. When an overpotential of -200 mV is applied, the current density of bare Zn anode keeps increasing for over 400 s, suggesting a random diffusion on the tips (**Figure 3h**).[28] In comparison, the Zn@TPZA electrode only delivers increased current density in the first 50 s for initial nucleation and then maintains a steady diffusion during Zn growth (**Figure 3i**).

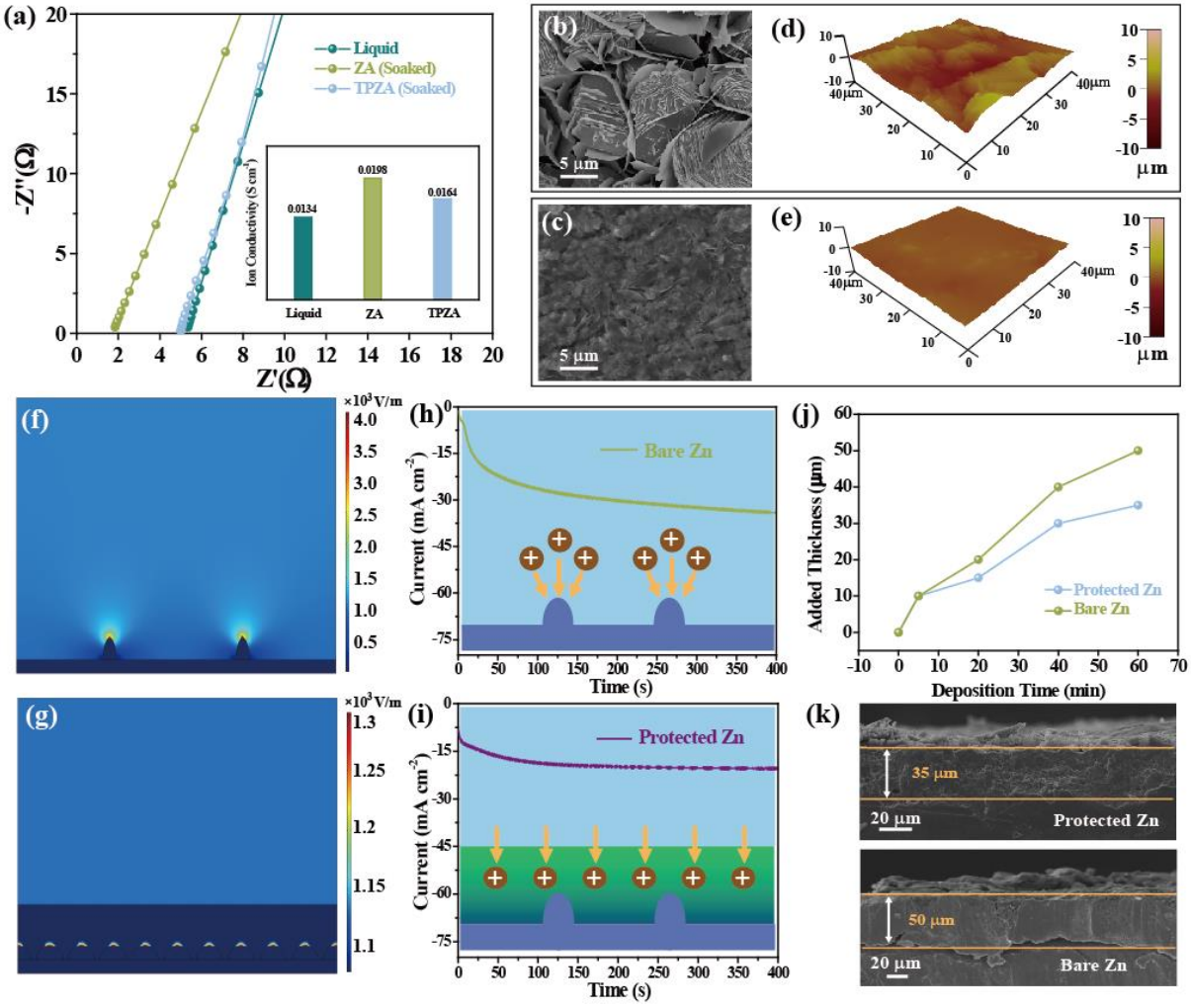

Figure 3. Zn deposition stability. (a) EIS of the liquid electrolyte, ZA layer and TPZA layer (with electrolyte soaked) in the frequency range from 10 kHz to 0.01 Hz. Morphology of (b) bare Zn and (c) Zn@TPZA with TPZA layer peeled off after 10 mAh cm^{-2} Zn deposition; 3D height images of (d) bare Zn and (e) Zn@TPZA with TPZA layer peeled off after 10 mAh cm^{-2} Zn deposition; Simulated electric field distribution for (f) bare Zn with protuberances and (g) Zn@TPZA with even deposited Zn seeds; Chronoamperometry curves at an overpotential of -200 mV and the illustration of Zn^{2+} diffusion for (h) bare Zn and (i) Zn@TPZA; (j) Thickness change for bare Zn and Zn@TPZA when Zn is deposited at10 mA cm^{-2}; (k) Cross-sectional SEM of deposited Zn with and without TPZA layer after 10 mAh cm^{-2} Zn deposition.

A remaining question regarding achieving high-capacity Zn anodes is the integrity of the interface subject to significant volume change. Note that the thickness of the electrode gradually increases with discharge capacity (**Figure 3j**). The thickness increases by ~50 μm cm^{-2} after 10 mAh cm^{-2} Zn deposition, much larger than the protected anode (~35 μm cm^{-2}). This proves that the TPZA layer induces a more dense Zn deposition. The SEM image (**Figure 3k**) indicates the interface is intact because of the excellent elasticity of the TPZA layer, and the Zn electrode is well protected with the newly deposited Zn grown underneath.

2.3 Cycling Stability and Reversibility of Zn@TPZA Anode.

The cyclic performance of symmetric cells Zn//Zn and Zn@TPZA//Zn@TPZA is conducted to evaluate the long-term stability of the interface under repeated Zn plating/stripping. At the current density of 2 mA cm^{-2} for a capacity of 2 mAh cm^{-2} (**Figure S12**), the voltage of Zn//Zn cells without protective coating suddenly drops after 190 h because of the short-circuit caused by dendrite evolution. In sharp contrast, the Zn@TPZA anode holds a particularly long and stable voltage curve for more than 1800 h. The electrode stability under high-power and high-capacity is necessitated for potential commercial application; thus, we examine the cells at more harsh conditions. Indeed, as shown in **Figure 4a-b**, the failure of the pristine Zn//Zn cell occurs more rapidly: ~140 h under 5 mA cm^{-2}/5 mAh cm^{-2} and merely ~60 h at 10 mA cm^{-2}/10 mAh cm^{-2} due to rampant dendrite accumulation and drastic volume change as having been widely reported. Surprisingly, the lifespan can be extended respectively to 1200 h and 500 h at 5 mA cm^{-2}/5 mAh cm^{-2} and 10 mA cm^{-2}/10 mAh cm^{-2} for Zn@TPZA cells. SEM image of the cycled bare Zn anode after failure exhibits a rough surface with a height difference of 10.9 μm (**Figure 4c** and **Figure S13a**), implying that dendrite growth is the leading cause of the short circuit. On the contrary, after cycling for 300 h, the Zn@TPZA retains a smooth morphology with a much smaller height difference of 1.2 μm (**Figure S14**). Even if the protecting layer is removed, the

flat morphology with a height difference of 3.8 μm can also be maintained (**Figure 4d** and **Figure S13b).**

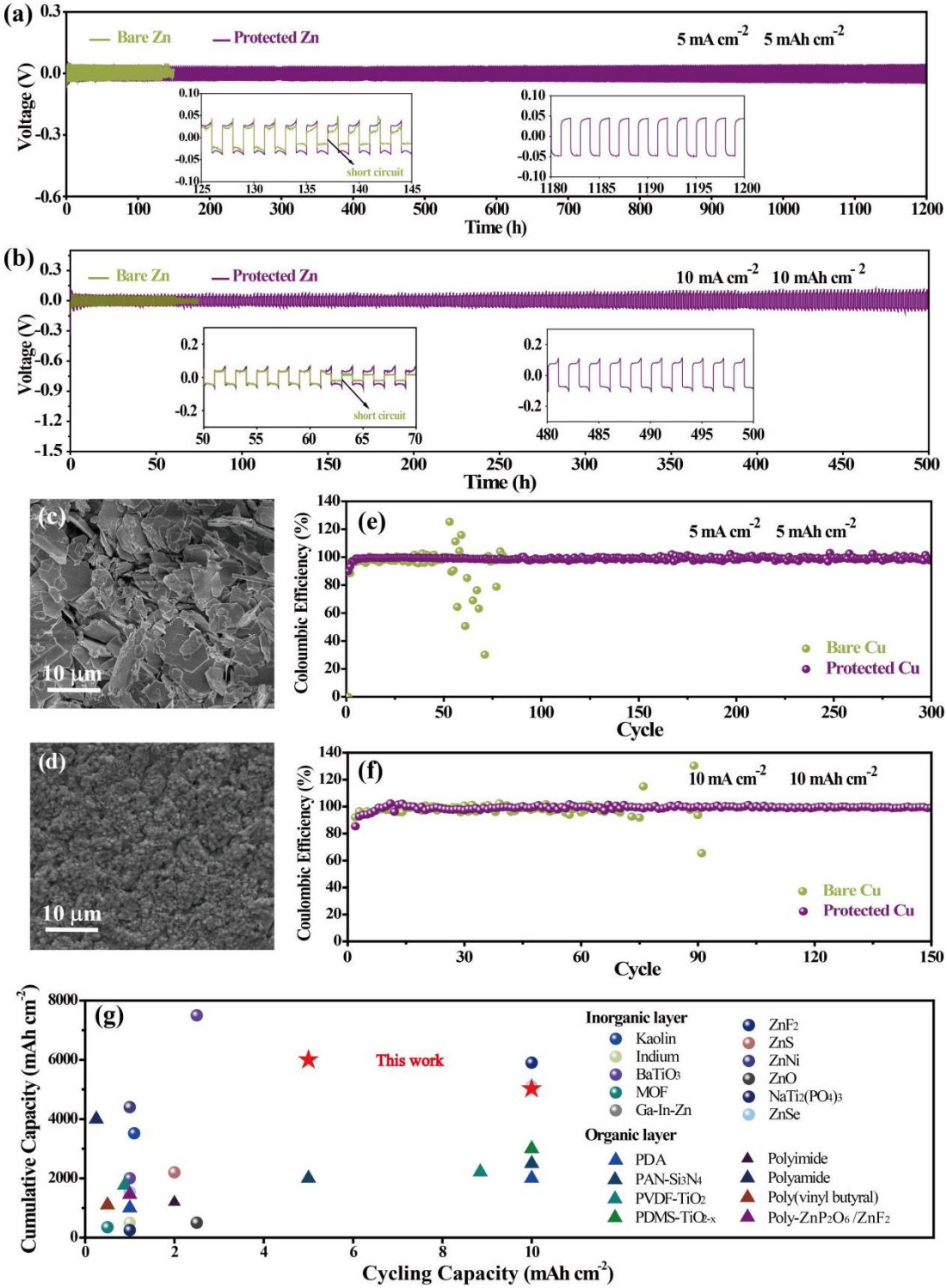

Figure 4. Cyclic stability of Zn anodes. Voltage profiles of bare Zn and Zn@TPZA anodes at (a) 5 mA cm^{-2}/5 mAh cm^{-2} and (b) 10 mA cm^{-2}/10 mAh cm^{-2}; SEM images of (c) bare Zn and

(d) Zn@TPZA with TPZA layer peeled off after cycling; Coulombic efficiency of the two anodes at (e) 5 mA cm^{-2}/5 mAh cm^{-2} and (f) 10 mA cm^{-2}/10 mAh cm^{-2}; (g) Comparison of cumulative capacity and cycling capacity of Zn@TPZA and other reported Zn anodes with various coating layers (Kaolin,[29] indium,[12] PDMS/TiO_2,[16] MOF,[30] polyamide,[31] ~~ZnF_2,~~[7] ZnS,[32] ZnO,[33] poly(vinyl butyral),[34] polyimide,[35] ZnSe,[5] PAN-Si_3N_4,[15] PVDF/TiO_2,[17] $BiTiO_3$,[36] $NaTi_2(PO_4)_3$,[37] Ga-In-Zn,[38] ZnNi[39], PDA,[40] Poly-ZnP_2O_6/ZnF_2[26])

It is worth noting that neither TPU nor Zn-Alg alone could realize the long cyclic stability at high rates (**Figure S15**). The cyclic life is reduced to 260 h at 10 mAh cm^{-2} for pure Zn-Alg coated Zn foil (Zn@ZA). Similarly, without the presence of Zn-Alg, the TPU grafted Zn (Zn@TPU) has a short lifespan of merely 78 h. It emphasizes the synergistic effect of the TPU elastic matrix and Zn-Alg filler in achieving long-term stability. Lastly, we examine the byproducts generation after long-term cycles (**Figure S16)**. Compared to the bare Zn, only a minor amount of $Zn_4SO_4(OH)_6 \cdot 3H_2O$ is detected on the Zn@TPZA electrode, again validating the anti-corrosion properties of the interface under cycling conditions.

Coulombic efficiency (CE) is a decisive factor in determining an anode's reversibility. It is obtained by calculating the plating/stripping capacity ratio, revealing the Zn loss in each cycle.[41] A Cu/Zn cell is assembled with the Cu and Zn foil serving as working and counter electrodes, respectively. A certain amount of Zn is firstly plated on Cu and then removed by charging to a cut-off voltage of 0.5 V. Without the protection of interface, the cell shows poor stability with CE fluctuating violently, and it fails in less than 100 cycles (**Figure S17**). We then fabricate the TPZA interface on the Cu foil (denoted as Cu@TPZA) as the working electrode. The CE of Cu@TPZA is stabilized at an average value of 98.63%, 99.05% and 99.47% at the cycling condition of 2 mA cm^{-2}/2 mAh cm^{-2} (**Figure S18**), 5 mA cm^{-2}/5 mAh cm^{-2} (**Figure 4e**) and 10 mA cm^{-2}/10 mAh cm^{-2} (**Figure 4f**), respectively, after a short activation process. The CE value obtained in this work is comparable to the prestigious works published

most recently (**Table S2**). The improved CE by the interface is attributed to several factors, including i) the inhibited Zn-consuming side reactions; and ii) the suppressed dendrite growth for reducing the dead Zn, which is mainly composed of the fractured dendrite debris that loses electric contact.

The performance of Zn@TPZA is compared with the art-of-the-state Zn anodes optimized by other similar interface-derived approaches. As shown in **Table S2** and **Figure 4g**, most of the reported interface protective Zn anodes focus on stability under relatively low current density, i.e., usually no more than 5 mA cm^{-2}. One of the reasons lies in the interface failure under a high current and high cycling capacity because of the enormous volume change and profound dendrite growth. We adopt the cumulative capacity, i.e., the product of cycling current and capacity, for a fair comparison. The Zn@TPZA has an impressive cumulative capacity at low current densities and maintains a high value at more challenging rates (6000 mAh cm^{-2} at 5 mA cm^{-2} and 5000 mAh cm^{-2} at 10 mA cm^{-2}), among the highest in the interface protected Zn anodes.

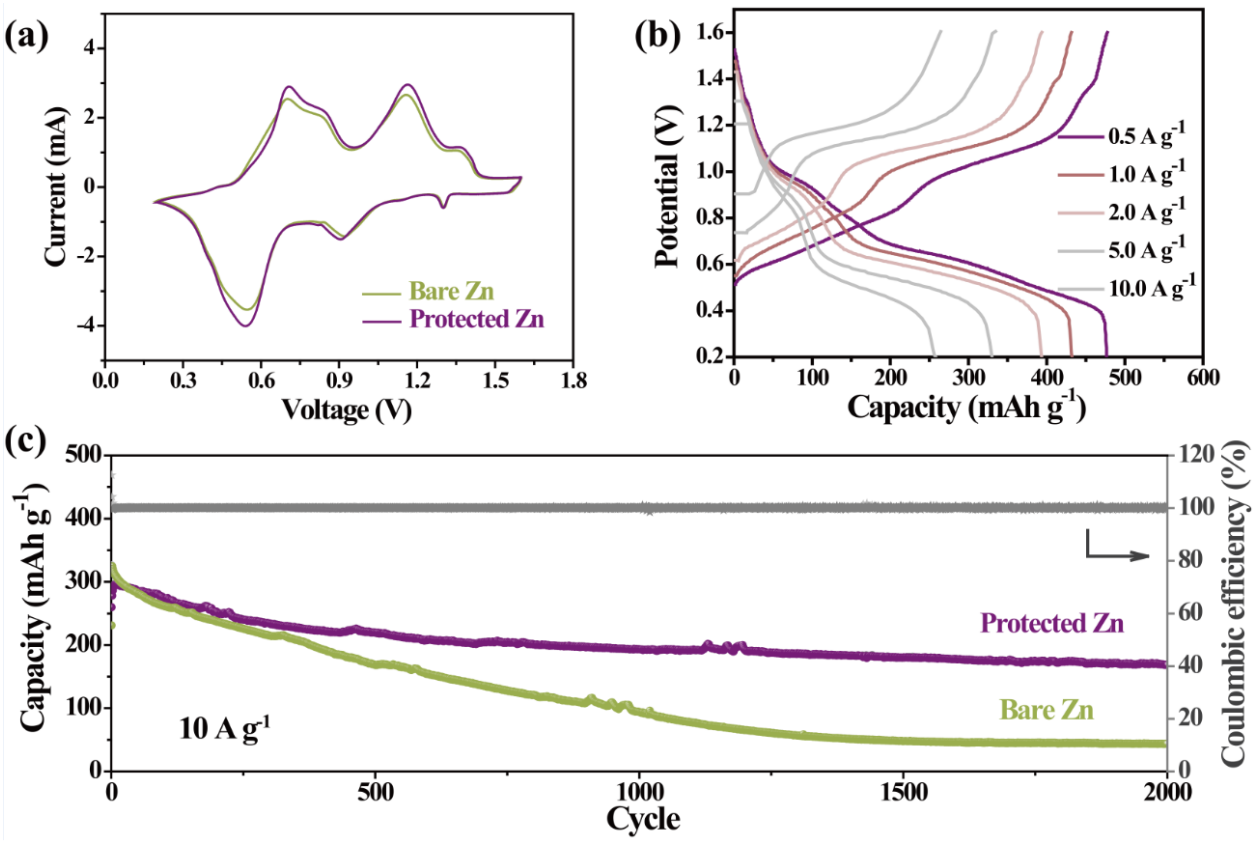

Figure 5. Full cell performance matched with a $Zn_xV_2O_5{\cdot}nH_2O$ cathode. (a) Comparison of CV curves at a scan rate of 0.5 mV s^{-1}; (b) GCD profiles at various current densities; and (c) Cyclic performance at 10 A g^{-1}.

2.4 Electrochemical Performance of Full Cells.

To assess the compatibly of the as-prepared interface with the cathode, we fabricate full cells by coupling the Zn or Zn@TPZA with a polyethylene glycol (PEG) modified vanadium-based compound (denoted as $Zn_xV_2O_5{\cdot}nH_2O$). The PEG-intercalation is adopted to enhance the stability of the $Zn_xV_2O_5{\cdot}nH_2O$ cathode, similar to the polyaniline (PANi) and polypyrrole (PPy)-modified ones.[42] As displayed in **Figure S19-S20**, the prepared cathode displays porous morphology and layered structure with an enlarged interlayer spacing, in line with the elemental mapping and XRD pattern.[43] The cathode exhibits a capacity of 476 mAh g^{-1} at 0.5 A g^{-1}, superior to most reported cathodes (**Table S3**). The CV profiles of two cells at the scan rate of 0.5 mV s^{-1} display two main pairs of cathodic/anodic peaks (**Figure 5a**), corresponding to the

redox couples of V^{4+}/V^{3+} and V^{5+}/V^{4+} associated with the Zn^{2+} insertion/extraction.[44] The similar CV shape confirms that the hybrid interface is stable during the electrochemical process without triggering side reactions. The cell with the Zn@TPZA shows a higher current response, indicating better electrochemical reaction activity. In addition, the full cell using bare Zn anode has a higher resistance after 10 cycles (**Figure S21**), which can be attributed to the formation of passivating byproducts, in agreement with the half-cell results. Turning to the rate performance, a capacity of 256 mAh g^{-1} can be achieved at a high current density of 10 A g^{-1} (**Figure 5b and Figure S22**). The elevated stability can also be demonstrated in long-term cyclic tests (**Figure 5c**). The full cell with Zn@TPZA anode exhibits superior stability, retaining a capacity of 168 mAh g^{-1} even after 2000 cycles at 10 A g^{-1}. In sharp contrast, the capacity decays to 43 mAh g^{-1} when a bare Zn is adopted. In addition, we use a pre-set amount of Zn as the anode to make the negative-to-positive electrode capacity (N:P) ratio of 5:1 (**Figure S23**). The discharge capacity of the corresponding full cell with the bare Zn anode deteriorates rapidly after about 80 cycles, showing a capacity of merely ~26 mAh/g after 200 cycles. On the contrary, the cell with protected Zn delivers a highly improved cycle stability of 200 cycles with a capacity of ~ 230 mAh/g maitained.

3. Conclusion

We design a novel matrix-filler hybrid interface to address the corrosion and dendrite issues of Zn metal anodes. The synergistic effect between the matrix and filler results in exceptional stability at concurrently high current rates and high cycling capacity, which has rarely been achieved in other similar interface-based strategies. For instance, the protected Zn anode delivers excellent durability of 1200 h at a current density of 5 mA cm^{-2} for the capacity of 5 mAh cm^{-2}. Such an achievement hinges on i) the anti-corrosion interface, which prevents the Zn-consuming H_2 evolution reactions and the formation of byproducts that increases the surface roughness; ii) the highly ionic conductive interface that facilitates the charge transfer and

induces the dendrite-free Zn growth underneath the interface; iii) the super-elastic matrix, which accommodates the drastic volume changes for allowing the large capacity cycling. This study unravels the critical features of an artificial interface for Zn metal anode and provides a feasible approach to build it through designing elastomer and ionic conductive polymer composites.

4. Experimental Section

Electrospinning of TPU matrix on Zn foil. A mixture of THF and DMF (volume ratio is 1:3) was prepared following the addition of 15 wt% TPU pellets. After stirring for 12 h, the homogeneous solution was injected into a syringe for the electrospinning. The whole process was performed under room temperature and ambient environment. The feeding rate of solution, needle-target distance, and applied voltage were set as 1 mL h^{-1}, 15 cm, and 12 kV, respectively. The as-obtained TPU nanofibers were collected by a cleaned Zn plate (thickness of 100 μm). Finally, the Zn@TPU plate was dried at 50 ℃ for 1 h for future usage.

Fabrication of Zn@TPZA anode. The as-prepared TPU/Zn foil was completely infiltrated by a 2 wt% sodium alginate aqueous solution and then transferred to a container with 2 M $ZnSO_4$ aqueous solution for Zn^{2+} crosslinking. After 6 h, the modified Zn anode was taken out for punching, assembling, and testing.

Preparation of Vanadium-based cathode. The $Zn_xV_2O_5{\cdot}nH_2O$ cathode was prepared by a modified hydrothermal method. Briefly, a transparent and homogeneous solution including 365 mg V_2O_5, 2 mL H_2O_2, 75 mg $Zn(NO_3)_2$, and 800 mg polyethylene glycol (PEG) was transferred into a 100 ml Teflon-lined autoclave and heated at 120 °C for 12 h. The black-green products were washed 3 times by DI water and ethanol through centrifugation and then vacuumed dried at 80 °C. Finally, the PEG modified $Zn_xV_2O_5{\cdot}nH_2O$ cathode was obtained.

Materials characterization. Scanning electron microscopy (SEM, Tescan VEGA3) was employed to check the surface morphology and elemental mappings of as-prepared anodes. The

infrared spectroscopy (IR) and phase structure were recorded by Fourier transform infrared (FT-IR) spectroscopy (Nicolet iS5) and X-ray diffraction (XRD, Rigaku Smartlab with Cu Kα radiation at 45 kV). X-ray photoelectron spectroscopy (XPS PHI 5600) was taken to examine the surface chemistry. The wettability of samples was measured by the contact angle measurement using a drop of electrolyte (2 M $ZnSO_4$) with a volume of 2 μL. The surface roughness was detected by AFM using a Bruker Icon Dimension XR system. The nanostructures and EDS mappings of the cathodes were explored by TEM (JEOL JEM-2100F).

Electrochemical measurements. The electrochemical behavior and cycling stability were performed by CR2032 coin-type cells with 2 M $ZnSO_4$ as electrolyte and GF/D glass fiber as the separator. The stripping/plating analysis of half cells was cycled at various current densities (2, 5 and 10 mA cm^{-2}) for corresponding capacities (2, 5 and 10 mAh cm^{-2}). The full cells were assembled with bare Zn or protected Zn as anode and $Zn_xV_2O_5{\cdot}nH_2O$ as the cathode. The working electrode was prepared by mixing $Zn_xV_2O_5{\cdot}nH_2O$ powder, super P, and poly(1,1-difluoroethylene) binder with a mass ratio of 7:2:1 in N-Methylpyrrolidone. Subsequently, the slurry was coated on a stainless substrate and vacuum dried for 12 h under 80 °C. The mass loading of the cathode was in the range of 1.4-1.6 mg. The CV curves were obtained at a scan rate of 0.5 mV s^{-1}, the Tafel plot was tested at a scan rate of 0.5 mV s^{-1}, and EIS was performed from 10^5 to 10^{-1} Hz with a potential amplitude of 5 mV. All of them were carried out on an electrochemical workstation (CHI760E). We use the EIS to measure the ionic conductivity (σ) of ZA and TPZA membrane after soaking with the liquid electrolyte. The experiment is carried out with two stainless steel sandwiching various membranes, including the electrolyte-soaked separator, ZA, and TPZA. The following formula: $\sigma=l/RS$ is adopted, where l and S are the thickness of the membrane and the contact area, respectively. The bulk resistance R is obtained from the intercept of the impedance curve on the x-axis.

Electric Field Simulation. A simplified two-dimensional model was constructed to simulate the electric field distribution at the interface between the anode and electrolyte based on Comsol

Multiphysics. In the entire model, the length and height of the Zn electrode were set as 60 μm and 2.5 μm, respectively. For pristine Zn, the protuberances on the surface were described as semicircles with a diameter of 2.5 μm and a height of 3 μm. For the modified anode, the thickness of the protective layer was set as 10 μm and the uniformly deposited Zn was described as semicircles with a diameter of 5 μm and a height of 2.5 μm due to the advanced effect of the hybrid layer. For boundary conditions, the anodic potential is 0 V, and the cathodic potential is determined by the voltage hysteresis (0.05 V) according to the experiment.

Supporting Information

Supporting Information is available from the Wiley Online Library or from the author.

Acknowledgements

This work was supported by the General Research Fund (GRF) scheme of the Hong Kong Research Grants Council (Project No. 15307221) and the Hong Kong Polytechnic University (ZVRP and ZE2F).

Conflict of Interest

The authors declare no conflict of interest.

Received: ((will be filled in by the editorial staff))
Revised: ((will be filled in by the editorial staff))
Published online: ((will be filled in by the editorial staff))

References

[1] a) M. Armand and J. M. Tarascon, *Nature* **2001**, *414*, 359; b) X. B. Cheng, R. Zhang, C. Z. Zhao and Q. Zhang, *Chem Rev* **2017**, *117*, 10403; c) Q. Liu, X. Hong, X. You, X. Zhang, X. Zhao, X. Chen, M. Ye and X. Liu, *Energy Storage Mater.* **2020**, *24*, 541.

[2] a) F. Wang, O. Borodin, T. Gao, X. Fan, W. Sun, F. Han, A. Faraone, J. A. Dura, K. Xu and C. Wang, *Nat. Mater.* **2018**, *17*, 543; b) J. Shin, J. Lee, Y. Park and J. W. Choi, *Chem. Sci.* **2020**, *11*, 2028.

[3] a) H. Pan, Y. Shao, P. Yan, Y. Cheng, K. S. Han, Z. Nie, C. Wang, J. Yang, X. Li, P. Bhattacharya, K. T. Mueller and J. Liu, *Nat. Energy* **2016**, *1*, 1; b) G. Fang, J. Zhou, A. Pan and S. Liang, *ACS Energy Lett.* **2018**, *3*, 2480; c) Y. Zhang, Z. Cao, S. Liu, Z. Du, Y. Cui, J. Gu, Y. Shi, B. Li, and S. Yang, Adv. Energy Mater. 2022, 2103979

[4] a) Z. Hou, Z. Lu, Q. Chen and B. Zhang, *Energy Storage Mater.* **2021**, *42*, 517; b) Z. Hou, Y. Gao, R. Zhou and B. Zhang, *Adv. Funct. Mater.* **2021**, 2107584; c) C. Huang, X. Zhao, S. Liu, Y. Hao, Q. Tang, A. Hu, Z. Liu and X. Chen, *Adv. Mater.* **2021**, *33*, e2100445; d) Y. An, Y. Tian, S. Xiong, J. Feng and Y. Qian, *ACS Nano* **2021**, 15, 11828; e) J. Hao, L. Yuan, C. Ye, D. Chao, K. Davey, Z. Guo and S. Z. Qiao, *Angew. Chem. Int. Ed. Engl.* **2021**, *60*, 7366; f) T. Wang, C. Li, X. Xie, B. Lu, Z. He, S. Liang and J. Zhou, *ACS Nano* **2020**, 14, 16321.

[5] X. Yang, C. Li, Z. Sun, S. Yang, Z. Shi, R. Huang, B. Liu, S. Li, Y. Wu, M. Wang, Y. Su, S. Dou and J. Sun, *Adv. Mater.* **2021**, 2105951.

[6] X. Xie, S. Liang, J. Gao, S. Guo, J. Guo, C. Wang, G. Xu, X. Wu, G. Chen and J. Zhou, *Energy Environ. Sci.* **2020**, *13*, 503.

[7] L. Ma, Q. Li, Y. Ying, F. Ma, S. Chen, Y. Li, H. Huang and C. Zhi, *Adv. Mater.* **2021**, *33*, e2007406.

[8] Q. Zhang, J. Luan, X. Huang, Q. Wang, D. Sun, Y. Tang, X. Ji and H. Wang, *Nat. Commun.* **2020**, *11*, 3961.

[9] L. Kang, M. Cui, F. Jiang, Y. Gao, H. Luo, J. Liu, W. Liang and C. Zhi, *Adv. Energy Mater.* **2018**, *8*, 1801090.

[10] P. Zou, R. Zhang, L. Yao, J. Qin, K. Kisslinger, H. Zhuang and H. L. Xin, *Adv. Energy Mater.* **2021**, *11*, 2100982.

[11] S. Li, J. Fu, G. Miao, S. Wang, W. Zhao, Z. Wu, Y. Zhang and X. Yang, *Adv. Mater.* **2021**, *33*, e2008424.

[12] D. Han, S. Wu, S. Zhang, Y. Deng, C. Cui, L. Zhang, Y. Long, H. Li, Y. Tao, Z. Weng, Q. H. Yang and F. Kang, *Small* **2020**, *16*, e2001736.

[13] A. Chen, C.Zhao, Z. Guo, X. Lu, N. Liu, Y. Zhang, L. Fan, N. Zhang, Energy Storage Mater. 2022, 44, 353.

[14] P. Bai, J. Li, F. R. Brushett and M. Z. Bazant, *Energy Environ. Sci.* **2016**, *9*, 3221.

[15] S. Zhou, Y. Wang, H. Lu, Y. Zhang, C. Fu, I. Usman, Z. Liu, M. Feng, G. Fang, X. Cao, S. Liang and A. Pan, *Adv. Funct. Mater.* **2021**, *31*, 2104361.

[16] Z. Guo, L. Fan, C. Zhao, A. Chen, N. Liu, Y. Zhang and N. Zhang, *Adv. Mater.* **2021**, e2105133.

[17] R. Zhao, Y. Yang, G. Liu, R. Zhu, J. Huang, Z. Chen, Z. Gao, X. Chen and L. Qie, *Adv. Funct. Mater.* **2020**, *31*, 2001867.

[18] J. Huang, D. Li, M. Zhao, A. Mensah, P. Lv, X. Tian, F. Huang, H. Ke and Q. Wei, *Adv. Electron Mater.* **2019**, *5*,1900241.

[19] C. Tao, M. H. Gao, B. H. Yin, B. Li, Y. P. Huang, G. Xu and J. J. Bao, *Electrochim. Acta* **2017**, *257*, 31.

[20] H. Zhang, R. Guo, S. Li, C. Liu, H. Li, G. Zou, J. Hu, H. Hou and X. Ji, *Nano Energy* **2022**, *92*, 106752.

[21] Y. Ding, X. Zhong, C. Yuan, L. Duan, L. Zhang, Z. Wang, C. Wang and F. Shi, *ACS Appl. Mater. Interfaces* **2021**, *13*, 20681.

[22] J. Mirtic, J. Ilas and J. Kristl, *Carbohydr. Polym.* **2018**, *181*, 93.

[23] D. Leal, B. Matsuhiro, M. Rossi and F. Caruso, *Carbohydr. Res.* **2008**, *343*, 308.

[24] D. Kundu, B. D. Adams, V. Duffort, S. H. Vajargah and L. F. Nazar, *Nat. Energy* **2016**, *1*, 1.

[25] S. H. Park, S. Y. Byeon, J. H. Park and C. Kim, *ACS Energy Lett.* **2021**, *6*, 3078.

[26] S. Liu, J. Mao, W. Pang, J. Vongsvivut, X. Zeng, L. Thomsen,Y. Wang, J. Liu, D. Li, Z. Guo, *Adv. Funct. Mater.* **2021**, 31, 2104281.

[27] X. Zeng, J. Mao, J. Hao, J. Liu, S. Liu, Z. Wang, Y. Wang, S. Zhang, T. Zheng, J. Liu, P. Rao, and Z. Guo, Adv.Mater. 2021, 33, 2007416.

[28] R. Zhou, H. Tan, Y. Gao, Z. Hou, X. Du and B. Zhang, *Carbon* **2022**, *186*, 141.

[29] C. Deng, X. Xie, J. Han, Y. Tang, J. Gao, C. Liu, X. Shi, J. Zhou and S. Liang, *Adv. Funct. Mater.* **2020**, *30*, 2000599.

[30] L. Cao, D. Li, T. Deng, Q. Li and C. Wang, *Angew. Chem. Int. Ed. Engl.* **2020**, *59*, 19292.

[31] Z. Zhao, J. Zhao, Z. Hu, J. Li, J. Li, Y. Zhang, C. Wang and G. Cui, *Energy Environ. Sci.* **2019**, *12*, 1938.

[32] J. Hao, B. Li, X. Li, X. Zeng, S. Zhang, F. Yang, S. Liu, D. Li, C. Wu and Z. Guo, *Adv. Mater.* **2020**, *32*, e2003021.

[33] J. Y. Kim, G. Liu, G. Y. Shim, H. Kim and J. K. Lee, *Adv. Funct. Mater.* **2020**, *30*, 2004210.

[34] J. Hao, X. Li, S. Zhang, F. Yang, X. Zeng, S. Zhang, G. Bo, C. Wang and Z. Guo, *Adv. Funct. Mater.* **2020**, *30*, 2001263.

[35] M. Zhu, J. Hu, Q. Lu, H. Dong, D. D. Karnaushenko, C. Becker, D. Karnaushenko, Y. Li, H. Tang, Z. Qu, J. Ge and O. G. Schmidt, *Adv. Mater.* **2021**, *33*, e2007497.

[36] K. Wu, J. Yi, X. Liu, Y. Sun, J. Cui, Y. Xie, Y. Liu, Y. Xia and J. Zhang, *Nano-Micro Lett.* **2021**, *13*, 79.

[37] M. Liu, J. Cai, H. Ao, Z. Hou, Y. Zhu and Y. Qian, *Adv. Funct. Mater.* **2020**, *30,* 2004885.

[38] H. Jia, Z. Wang, M. Dirican, S. Qiu, C. Y. Chan, S. Fu, B. Fei and X. Zhang, *J. Mater. Chem. A* **2021**, *9*, 5597.

[39] P. Cao, J. Tang, A. Wei, Q. Bai, Q. Meng, S. Fan, H. Ye, Y. Zhou, X. Zhou and J. Yang, *ACS Appl. Mater. Interfaces* **2021**, *13*, 48855.

[40] X. Zeng, K. Xie, S. Liu, S. Zhang, J. Hao, J. Liu, W. Pang, J. Liu, P. Rao, Q. Wang, J. Mao and Z. Guo, *Energy Environ. Sci.* **2021**, 14, 5947.

[41] Z. Hou, Y. Gao, H. Tan and B. Zhang, *Nat. Commun.* **2021**, *12*, 3083.

[42] S. Liu, H. Zhu, B. Zhang, G. Li, H. Zhu, Y. Ren, H. Geng, Y. Yang, Q. Liu and C. Li, Adv. Mater. 2020, 32, 2001113.

[43] Y. Yang, Y. Tang, G. Fang, L. Shan, J. Guo, W. Zhang, C. Wang, L. Wang, J. Zhou and S. Liang, *Energy Environ. Sci.* **2018**, *11*, 3157.

[44] (a) W. Zhong, J. Huang, S. Liang, J. Liu, Y. Li, G. Cai, Y. Jiang and J. Liu, *ACS Energy Lett.* **2019**, *5*, 31; (b) J. Ding, Z. Du, B. Li, L. Wang, S. Wang, Y. Gong and S. Yang, Adv. Mater. 2019, 31, 1904369